2013 IEEE/RSJ International Conference on
Intelligent Robots and Systems (IROS)
September 14-18, 2014. Chicago, IL, USA,

Recursive Estimation of Needle Pose for Control of 3D-Ultrasound-Guided Robotic Needle Steering

Troy K. Adebar and Allison M. Okamura

***Abstract*— Robotic systems can improve percutaneous interventions by steering flexible needles along nonlinear trajectories. These systems require medical image feedback for accurate closed-loop control. Three-dimensional (3D) ultrasound can provide real-time measurements of needle pose within tissue; however, the ultrasound produces relatively large amounts of measurement noise. A recursive estimation approach is described for accurately estimating the six-degree-of-freedom pose of a steerable needle tip, by applying an unscented Kalman filter (UKF) to 3D ultrasound segmentation results. The UKF is formulated based on a kinematic process model of needle steering, as well as experimental quantification of the statistical variability of steering and imaging needles in biological tissue. Validation testing shows that the UKF method makes accurate closed-loop robotic control of the needle tip possible in biological tissue. Compared to direct use of noisy ultrasound data for control feedback, the UKF reduced average positioning error by 9.58 mm (81%) when steering towards a simulated target. This new estimation scheme will contribute towards the future evaluation of needle steering robots in real-world clinical applications.**

I. INTRODUCTION

Percutaneous interventions are hyper-minimally invasive medical procedures that use needles to access targets within the body. Example applications include biopsy, ablation, cryotherapy, targeted drug delivery, and brachytherapy. While such percutaneous procedures are applied throughout medicine, they are all limited by the fact that current needles can only be inserted along straight paths. Accessing multiple targets thus requires multiple needle insertions, with each insertion causing trauma to the patient and increasing the risk of complications. In addition, vulnerable structures (*e.g.*, nerves, blood vessels, organs) or impassable obstacles (*e.g.*, bony structures, tough connective tissues) can prevent straight-line access to some targets.

Robotic needle steering is a concept that can potentially allow percutaneous interventions to overcome these limitations. (A recent survey of needle steering literature can be found in [1].) In this approach, a robotic system, such as the one shown in Fig. 1, steers a needle along a controlled curved path through tissue, allowing access to multiple targets through a single puncture wound, and to targets blocked by obstacles. The steering effect can be generated through several methods, including independent robotic control of overlapping prebent needle sections, external robotic manipulation of tissue, and mechanical actuation of needle sections. In our work, we apply asymmetric-tip needle steering. In this technique, an extremely flexible metal wire with an asymmetric tip (generally a beveled cutting tip in combination with an angled distal section) curves naturally along an approximately circular path as a result of the lateral force acting on the tip during insertion into tissue. The direction of this circular path can be controlled by rotating the needle at its base during insertion.

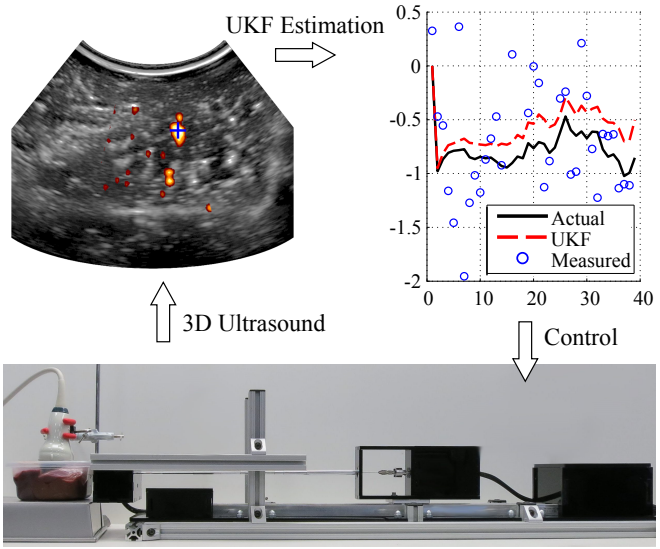

Fig. 1. Overview of 3D-ultrasound-guided robotic needle steering and filtering concept. An unscented Kalman filter is applied to noisy 3D ultrasound segmentation results to improve closed-loop control of a needle steering robot. The robot steers the needle tip to a target within a sample of *ex vivo* porcine liver tissue.

Robotic needle steering is a well-developed research area, with a rich prior art covering topics such as kinematic modeling, path planning and robot control. However, this prior work has generally focused on development of theoretical models and control schemes, with experimental validation performed in highly constrained, unrealistic settings. For example, validation of image-guided needle steering methods has mostly been performed in thin slabs of transparent rubber or gelatin, with optical cameras used to track the needle in place of medical imaging. Many important engineering problems must still be solved to allow *in vivo* testing to evaluate the clinical value of needle steering. The focus of our current work is the development of practical methods for medical-image-guided needle steering.

Previous image-guided control schemes for robotic needle steering have been derived from either a kinematic model

*This work was supported by the National Sciences and Engineering Research Council of Canada (student fellowship), and Stanford University.

T. K. Adebar and A. M. Okamura are with the Department of Mechanical Engineering, Stanford University, Stanford, CA, 94305, {tadebar,aokamura}@stanford.edu.

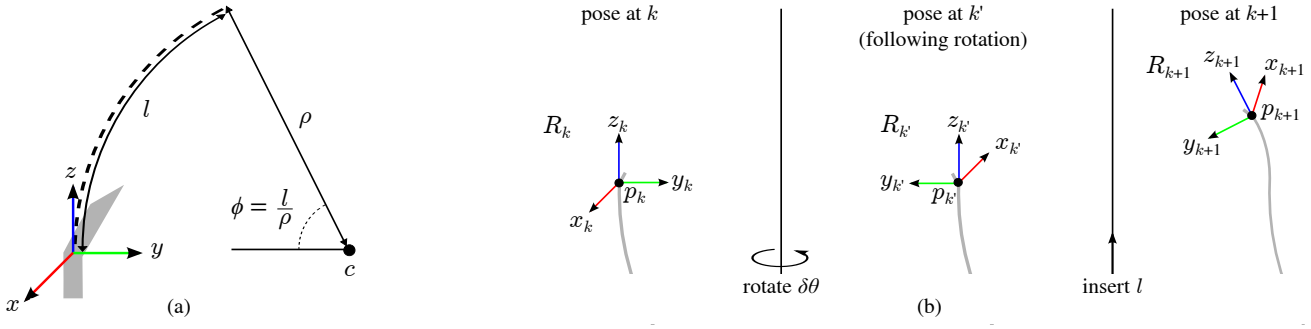

Fig. 2. Kinematic model of needle steering [2] used in image-guided control: (a) Needle tip frame. The z-axis is tangent to the needle at the tip (ignoring the bevel or prebent section), the y-axis points towards the center of curvature. The needle path is an arc within the y-z plane with radius ρ and arc length l. (b) Progression of the needle tip frame during steering. The steerable needle insertion is divided into increments, with incremental needle rotation angle ($\delta\theta$), incremental insertion distance (l) and radius of curvature (ρ) updated as command inputs between increments. These command inputs define the transition of state vector $\boldsymbol{x}$.

of curved needle paths, or a mechanical model of needle-tissue deflection. Several schemes have been described for combining 2D motion planning algorithms [3], [4], [5] with low-level controllers that hold the needle tip within a specific 2D plane [6], [7]. These motion planning algorithms are used to control the curvature of asymmetric-tip needles within the 2D plane in a binary sense (*i.e.*, curve up or curve down). Other methods have been described that use X-ray imaging [8] and 2D ultrasound imaging [9], [10] to track the needle and update the parameters of a mechanical model. The model is then used to solve for the control inputs needed to reach a target. All the described control schemes have involved needle steering and imaging within a single 2D plane, mainly because of the difficulty of imaging thin, curved, steerable needles with 3D medical imaging modalities such as MRI, CT, or 3D ultrasound. Since it is unlikely that needle steering within a single plane would be acceptable in a realistic clinical application, further development of methods for 3D imaging and control is needed. Electromagnetic (EM) tracking systems could possibly be used to track needle tip pose in place of medical imaging; however, interference from metal objects and EM noise can limit these systems in clinical settings. Furthermore, medical imaging is still required to track the motion of anatomic targets as the needle is steered through tissue.

We recently described a method for using high-frequency vibration to highlight steerable needles in 3D Doppler ultrasound [11]. Segmentation of the needle from the 3D Doppler ultrasound data can be accomplished using simple image analysis techniques, unlike standard B-mode (gray-scale) ultrasound data which generally yield very poor needle visibility and require complex segmentation techniques. While we demonstrated that this approach can reveal the curved shape of the needle, the resulting measurement of needle tip pose is quite noisy relative to the desired precision of needle steering. (Clinicians using medical image guidance systems can manually position needle tips within approximately 2 mm of a target in relevant interventions [12].)

To compensate for noise in the needle measurements generated by the Doppler ultrasound, we describe in this paper a recursive estimation scheme using an unscented Kalman filter based on a nonlinear kinematic model of needle steering. This filter relies on an experimental quantification of process and measurement noise for ultrasound-guided needle steering in biological tissue, which was performed using an electromagnetic tracking system as a reference. To evaluate our estimation scheme, a needle steering robot incorporating the UKF was compared with a robot relying directly on unfiltered ultrasound data. This work is the first demonstration of 6 degree-of-freedom (DOF) steerable needle tip pose estimation based on a 3D medical imaging modality, and represents an important step towards the future deployment of image-guided robotic needle steering in a clinical setting.

II. METHODS

A. Needle Steering Model

Our kinematic model of needle steering is based on the unicycle model [2]; we assume the needle travels along curved paths that are tangent to each other. To begin, we define the needle tip frame. As shown in Fig. 2, this frame is attached to the tip of the steerable needle, and oriented so that its z-axis is tangent to the needle at the tip, and its y-axis points towards the center of curvature. In this model, the state of the needle is described by the pose of the needle tip frame relative to a reference frame, in our case the 3D ultrasound frame.

1) Needle State Representation: Needle tip position is represented by a vector $\boldsymbol{p} \in \mathbb{R}^3$. There are several possible representations of tip orientation, including quaternions, Euler angles, and direction cosine matrices (rotation matrices). We have elected to use an axis-angle vector $\boldsymbol{r} \in \mathbb{R}^3$, where the magnitude of $\boldsymbol{r}$ represents the magnitude of rotation, and the direction of $\boldsymbol{r}$ represents the axis of rotation. This is a singularity-free representation with the advantage that it exists in a vector space, so the mean and covariance of multiple rotations are straightforward to calculate. To describe sequential rotations in the state transition equations, we will frequently use the equivalent rotation matrix representation for vector $\boldsymbol{r}$, $\boldsymbol{R} \in \mathrm{SO}(3)$, which can be calculated directly

from $\boldsymbol{r}$. The state vector $\boldsymbol{x} \in \mathbb{R}^6$ is thus defined as

$$\boldsymbol{x} = \begin{bmatrix} \boldsymbol{p} \\ \boldsymbol{r} \end{bmatrix} = \begin{bmatrix} p_0 & p_1 & p_2 & r_0 & r_1 & r_2 \end{bmatrix}^{\mathrm{T}}. \quad (1)$$

2) State Transition Model: Based on the kinematic model of needle steering [2], we define the transition of needle state to the next time interval, $\boldsymbol{x_{k+1}}$, as a function of the current state, $\boldsymbol{x_k}$, a vector of command inputs, $\boldsymbol{u_k}$, and a vector of process noise, $\boldsymbol{w}$:

$$\boldsymbol{x_{k+1}} = f(\boldsymbol{x_k}, \boldsymbol{u_k}, \boldsymbol{w}). \quad (2)$$

In our model, we divide needle steering into incremental insertions. Command inputs are applied between incremental insertions, and include change in needle base rotation $\delta\theta$, incremental insertion distance l, and radius of incremental needle path ρ:

$$\boldsymbol{u} = \begin{bmatrix} \delta\theta & l & \rho \end{bmatrix}^{\mathrm{T}}. \quad (3)$$

The radius of the needle path can be adjusted using duty cycling [13], [14], a control approach that uses short, variable periods of insertion with and without rotation to adjust needle curvature from maximum curvature to straight. System variability is modeled using nonadditive Gaussian noise in the state transition model. The noise vector $\boldsymbol{w} \in \mathbb{R}^6$ can be separated into a position component, $\boldsymbol{p_w} \in \mathbb{R}^3$, and an orientation component, $\boldsymbol{r_w} \in \mathbb{R}^3$. The index k is omitted from the vector $\boldsymbol{w}$ to signify the random nature of the vector.

The state transition function f can be viewed as a transformation of the tip frame, as shown in Fig. 2. The needle tip frame at time k has pose defined by $\boldsymbol{p_k}$ and $\boldsymbol{R_k}$. The needle tip frame is first rotated about its z-axis by $\delta\theta$ to yield the rotated tip frame:

$$\boldsymbol{R_{k'}} = \boldsymbol{R_k}\boldsymbol{Rz}(\delta\theta). \quad (4)$$

The needle is then inserted a distance l, with the tip following a circular path of radius ρ. From the definition of the tip frame shown in Fig. 2, we know that the needle path will lie in the y-z plane of the rotated frame defined by $\boldsymbol{R_{k'}}$. The position of the needle tip after insertion relative to the rotated frame can be found directly from the geometry of the circular path:

$${}^{\boldsymbol{k'}}\boldsymbol{p_{k+1}} = \begin{bmatrix} 0 \\ \rho(1 - \cos(\frac{l}{\rho})) \\ \rho \sin(\frac{l}{\rho}) \end{bmatrix}. \quad (5)$$

Transforming this vector into the world frame, and including process noise yields an expression for p_{k+1}:

$$\boldsymbol{p_{k+1}} = \boldsymbol{R_k}\boldsymbol{Rz}(\delta\theta)^{\boldsymbol{k'}}\boldsymbol{p_{k+1}} + \boldsymbol{p_k} + \boldsymbol{p_w}. \quad (6)$$

The orientation of the tip frame after insertion can be defined using the same rotation matrices. Similar to other studies that have applied Kalman filters to orientation representations [15], we include orientation noise as an initial disturbance to the state vector, $\boldsymbol{R_w}$. The updated tip frame orientation is thus

$$\boldsymbol{R_{k+1}} = \boldsymbol{R_k}\boldsymbol{R_w}\boldsymbol{Rz}(\delta\theta)\boldsymbol{Rx}\left(-\frac{l}{\rho}\right). \quad (7)$$

The vector $\boldsymbol{r_{k+1}}$ is the rotation vector equivalent of $\boldsymbol{R_{k+1}}$.

3) Measurement Model: Based on our 3D ultrasound needle segmentation method [11], we define the measurement model as full-state feedback with additive measurement noise vector $\boldsymbol{v}$:

$$\boldsymbol{z_k} = \boldsymbol{x_k} + \boldsymbol{v}. \quad (8)$$

This model assumes that the needle segmentation method can measure the full 6DOF pose of the needle tip frame. Although rotation around the axis of a needle can not generally be resolved by 3D ultrasound, in the case of a curved steerable needle we can use the direction of needle curvature to estimate the y-axis of the needle frame.

B. Unscented Kalman Filter

The unscented Kalman Filter is an extension of the classical Kalman filter to nonlinear systems, and uses a set of sampled points around a mean value to represent distributions [16]. For brevity, we will omit a detailed description of the unscented Kalman filter algorithm, and refer the reader to [17] for a complete explanation. Our implementation of the unscented Kalman filter uses the default values of the weighting parameters, $\alpha = 0.001$, $\xi = 0$, $\beta = 2$, and follows the original description of the algorithm [16] with one exception. Since the effect of process noise on the state transition is nonadditive, we include the noise covariance matrix Q (described in the next section) in the generation of the Sigma points, as suggested in [15].

C. Experimental Methods

1) Quantification of Process and Measurement Noise: Application of the UKF requires an understanding of the relative amounts of uncertainty (*i.e.*, noise) in the evolution of the state (process noise) and the measurement of the state (measurement noise). To quantify the process and measurement noise involved in 3D-ultrasound-guided needle steering, we performed experimental measurements using samples of *ex vivo* porcine liver tissue, as shown in Fig. 1, to simulate human tissue.

Process noise was quantified by using a magnetic tracking system to precisely measure the motion of a steerable needle tip during incremental insertion along constant curvature paths. A hollow steerable needle 0.80 mm in diameter was connected to the needle steering robot shown in Fig. 1, and a 6DOF sensor attached to a magnetic tracking system (driveBAY; Ascension Technology Corp., Milton, VT) was inserted into the needle tip. The pose of the needle tip after each incremental step was compared with what was expected based on the previous pose and the process model. Denoting the state vector measured by the magnetic tracking system as $\hat{\boldsymbol{x}}$, we determined an error vector $\boldsymbol{w}$ at each step such that

$$\hat{\boldsymbol{x}}_{\boldsymbol{k+1}} = f(\hat{\boldsymbol{x}}_{\boldsymbol{k}}, \boldsymbol{u}_{\text{est}}, \boldsymbol{w}). \quad (9)$$

During these experiments, input vector $\boldsymbol{u}_{\text{est}}$ was held constant at $[0, 3 \text{ mm}, \rho_{\text{est}}]^T$. The needle was inserted along four paths, with between fifteen and twenty measured positions per path. Initial tip frame orientation was measured by fitting a circular arc to the set of measured positions, and identifying the

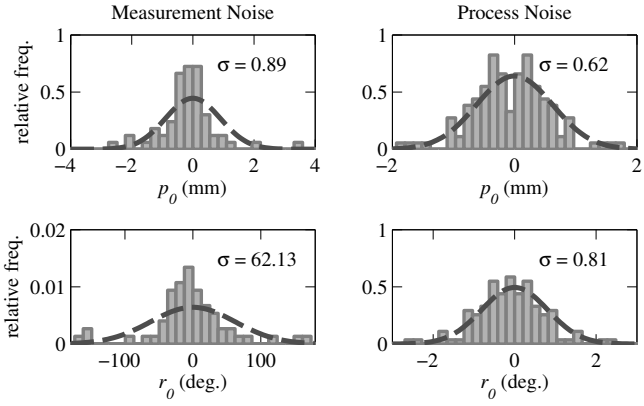

Fig. 3. Distributions of process and measurement noise for p_0 and r_0 components of position and orientation. Histograms of experimentally measured error vectors (gray bars) are compared with the normal distributions used in needle steering simulations.

vectors tangent (z-axis) and normal (x-axis) to the arc at the initial tip position. Data analysis was performed offline using Matlab.

Measurement noise was quantified by comparing automatic segmentation results from repeated 3D ultrasound scans of steerable needles in biological tissue. Between five and eleven repeated scans were performed for each of six needle tip poses. The needles were automatically segmented from each scan using the previously described Doppler method [11]. In this method, high-frequency vibration applied to a steerable needle yields an irregular outline of the needle in ultrasound Doppler data, whereas the needle is often not visible at all in standard B-mode ultrasound data. Data analysis was again performed offline in Matlab.

2) 3D-Ultrasound-Guided Needle Steering Simulations: We first evaluated our UKF algorithm in a series of simulated closed-loop needle steering trials. These simulations allowed us to compare our UKF results with the true needle tip state, which was not possible in the experiments described in the next section. In each trial, a target tip position and initial tip pose were identified in the 3D ultrasound coordinate system, and the needle tip was steered towards the target along a 3D path. Four initial scans were simulated to allow the UKF estimate to converge. Afterwards, the needle was steered in constant 3-mm incremental insertions using the UKF-filtered segmentation results to correct the needle rotation and path radius settings at each step. To provide a comparison baseline, each trial was also repeated using the unfiltered segmentation results as control feedback.

The target point $\boldsymbol{t}$ was varied according to a uniform distribution:

$$\boldsymbol{t} \sim U\left(\begin{bmatrix}-20\\35\\30\end{bmatrix}, \begin{bmatrix}20\\65\\60\end{bmatrix}\right). \tag{10}$$

Initial needle tip position was held constant:

$$\boldsymbol{p}_{\text{init}} = \begin{bmatrix}0 & 50 & -40\end{bmatrix}^{\text{T}}.$$

Initial needle tip orientation was varied according to a normal distribution:

$$\boldsymbol{r}_{\text{init}} \sim N\left(\begin{bmatrix}0\\0\\0\end{bmatrix}, \begin{bmatrix}32.82 & 0 & 0\\0 & 32.82 & 0\\0 & 0 & 32.82\end{bmatrix}\right). \tag{11}$$

Simulations were implemented in Matlab.

3) 3D-Ultrasound-Guided Needle Steering Experiments: In addition to simulation tests, we performed a series of closed-loop needle steering experiments. The robot shown in Fig. 1 steered a 0.58 mm needle with a bevel tip in *ex vivo* porcine liver tissue under 3D ultrasound guidance. The UKF algorithm was implemented in C++ and combined with algorithms for Doppler image segmentation. A SonixMDP ultrasound console (Ultrasonix Medical Corp., Richmond, Canada) with a convex mechanical 3D transducer (4DC7-3/40) was used for imaging. Similar to the simulated trials, a target was defined in the 3D ultrasound coordinate system and the needle was steered in constant 5-mm incremental insertions using sensor feedback to correct the needle rotation and path radius settings at each step. For comparison, six steering tests each were performed with and without the UKF.

III. RESULTS

A. Quantification of Process and Measurement Noise

Across 66 samples of process noise, the mean (in millimeters and degrees) was

$$\boldsymbol{\mu_w} = \begin{bmatrix}0.38 & -0.09 & 0.17 & 0.43 & 0.02 & 0.50\end{bmatrix}^{\text{T}}.$$

To find the best-fit zero-mean Gaussian distribution to the process noise, we reflected the measured noise vectors, resulting in a sample covariance of

$$\hat{\boldsymbol{Q}} = \begin{bmatrix}0.39 & -0.06 & 0.15 & 0.24 & -0.05 & 0.08\\ -0.06 & 0.21 & -0.10 & -0.17 & 0.17 & -0.05\\ 0.15 & -0.10 & 0.16 & 0.09 & -0.08 & 0.23\\ 0.24 & -0.17 & 0.09 & 0.65 & -0.34 & -0.09\\ -0.05 & 0.17 & -0.08 & -0.34 & 1.22 & 0.00\\ 0.08 & 0.05 & 0.23 & -0.09 & 0.00 & 2.49\end{bmatrix}.$$

In the measurement noise experiment, we assumed the mean of repeated segmentations at each tip pose was the true needle pose. This was necessary because we did not have a reference segmentation method for comparison (thin steerable needles are not generally visible in B-mode ultrasound). Across 60 observations of measurement noise, the sample covariance was

$$\hat{\boldsymbol{R}} = \begin{bmatrix}0.81 & 0.09 & -0.27 & 3.41 & 37.1 & 18.2\\ 0.09 & 1.10 & 0.51 & -17.7 & 20.2 & 4.97\\ -0.27 & 0.51 & 0.90 & -13.5 & 1.54 & -3.68\\ 3.41 & -17.7 & -13.5 & 3930 & -1720 & -375\\ 37.1 & 20.2 & 1.54 & -1720 & 7520 & 2740\\ 18.2 & 4.97 & -3.68 & -375 & 2740 & 1240\end{bmatrix}.$$

These experimental results give an indication of the relative levels of process and measurement noise, which is valuable for a Kalman filter formulation; however, only a relatively small number of measurements were practical for both experiments, and as a result it is difficult to infer characteristics of the underlying distributions. On the other hand, the process noise measurements, which were correlated and had non-zero mean, suggest that the kinematic model

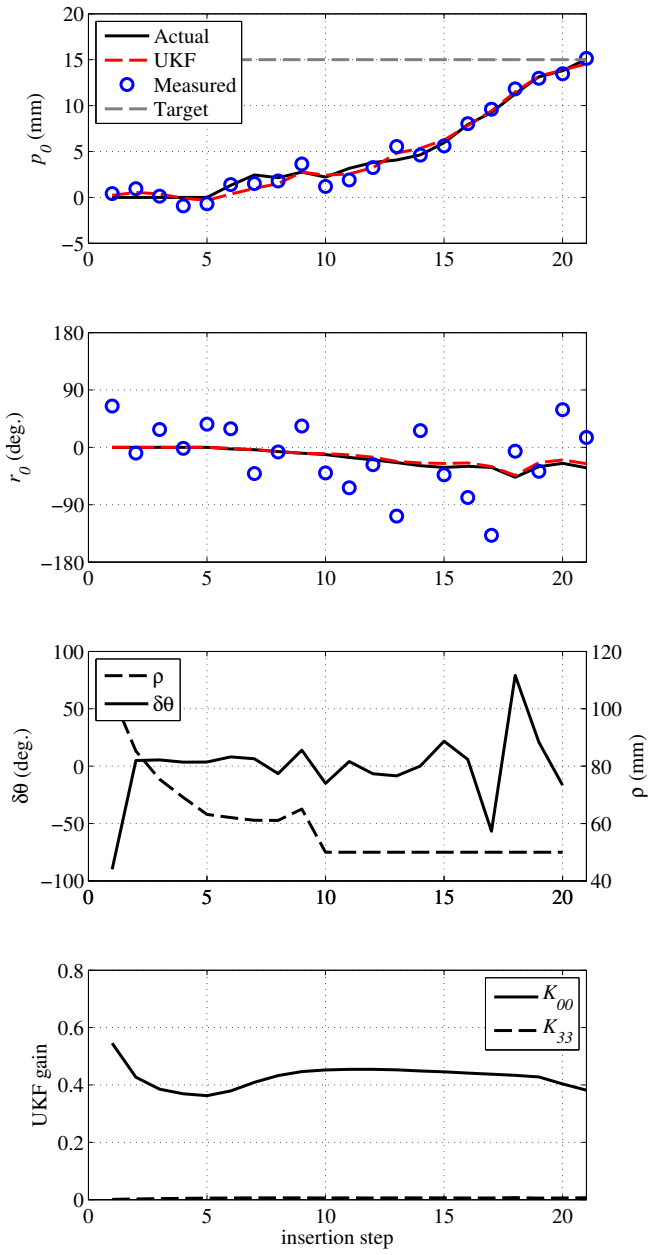

Fig. 4. Closed-loop needle steering results. Actual, measured and UKF-estimated state vector elements p_0 and r_0 are shown for steering towards a target located at $p_0 = 15$. The resulting values of control variables $\delta\theta$ and ρ are also plotted, and represent the control effort needed to overcome process variability inherent to steering in biological tissue. UKF gain values K_{00} and K_{33} show significant reliance on measured needle position, but relatively little reliance on measured needle orientation when forming the UKF estimate.

of needle steering we applied may not completely capture needle behavior in *ex vivo* liver. While a more sophisticated bicycle model of needle kinematics exists [2], it is identical to the unicycle model except when rotating the needle, which we did not do in our process noise experiments. With a more accurate kinematic model, we would expect the process noise to approximately follow a normal distribution with zero mean. This process noise would describe small deflections of the needle tip off the expected trajectory that would

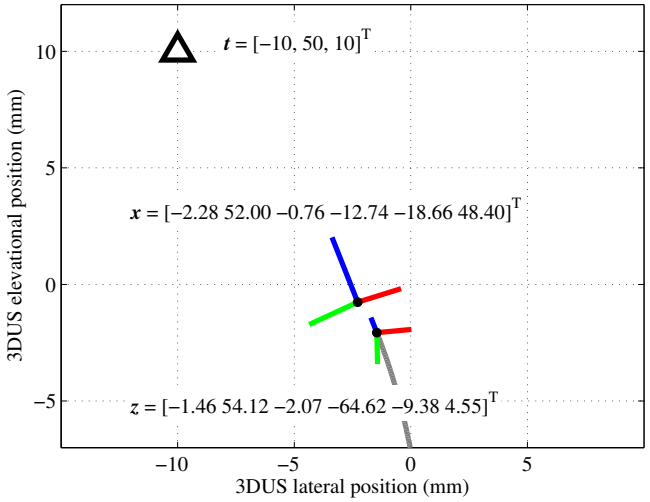

Fig. 5. Experimental results for closed-loop needle steering in *ex vivo* porcine liver tissue. After seven iterations, the UKF estimate of needle pose $\boldsymbol{x}$ (large axes) has less error in orientation than the measured needle pose $\boldsymbol{z}$ (small axes), which is based entirely on the segmented needle curve (solid line). The robot continued steering towards the target point $\boldsymbol{t}$, and achieved final tip placement error of 2.67 mm.

TABLE I

TIP PLACEMENT ERRORS IN NEEDLE STEERING EXPERIMENTS

Test	1	2	3	4	5	6	avg.
UKF (mm)	2.67	2.34	3.83	3.44	2.90	0.98	2.69
No UKF (mm)	9.89	13.41	9.03	11.12	10.14	14.74	11.39

result from steering in an inhomogeneous biological material. The difference in the experimental measurements suggests further investigation is warranted. Fig. 3 shows experimental histograms of process and measurement noise for the first components of position and orientation (*i.e.*, p_0 and r_0) compared to normal distributions with the same variance. In our needle steering simulations, we modeled the process and measurement noise as normally distributed, with zero mean and covariance equal to $\hat{\boldsymbol{Q}}$ and $\hat{\boldsymbol{R}}$ as defined above.

To make our simulations realistic, we chose to formulate the Kalman gains in the UKF without exact knowledge of the process or measurement noise distributions. Specifically, the UKF assumed both process and observation noise were uncorrelated and normally distributed with zero mean and variances of

$$\boldsymbol{Q} = \text{diag}(\begin{bmatrix}0.2 & 0.2 & 0.2 & 3.28 & 3.28 & 3.28\end{bmatrix}^T),$$

$$\boldsymbol{R} = \text{diag}(\begin{bmatrix}1 & 1 & 1 & 3282 & 3282 & 3282\end{bmatrix}^T).$$

B. 3D-Ultrasound-Guided Needle Steering Simulations

Over 10,000 simulation trials, the average error (mean $\pm$ standard deviation) in final tip placement was 2.26 $\pm$ 1.30 mm using the UKF-filtered segmentation results for feedback, and 11.85 $\pm$ 7.36 mm using the unfiltered segmentation results. Based on a bootstrapped statistical test, the UKF resulted in a statistically significant increase in placement accuracy ($p < 0.01$).

Fig. 4 shows simulation results from using the UKF-filtered segmentation data in closed-loop steering towards a target. The figure shows actual, measured and estimated values for two state elements (again p_0 and r_0), along with resulting control inputs ($\delta\theta$ and ρ) and UKF gains. In this simulation, the needle tip was steered from a point with $p_0 = 0$ towards a point at $p_0 = 15$. As seen in the figure, the UKF approach accurately estimated the true position and orientation despite large amounts of measurement noise, particularly in orientation. As mentioned above, the segmentation method we apply is based on measuring the centroid of irregular Doppler patches around the needle, and gives a relatively poor indication of needle tip orientation. The UKF estimate of tip orientation was thus based almost entirely on our kinematic model of needle steering, whereas the UKF estimate of tip position was based on both the kinematic model and the segmentation results. This is shown by the UKF gains K_{00} and K_{33}, which represent how heavily measurements z_0 and z_3 are weighted versus the corresponding process model outputs at each iteration. As shown by the control inputs, the robot made a large initial rotation to steer the needle towards the target, then made small corrections as a result of the steering variability (process noise). Once the needle approached the target, larger rotations and tighter path radii were necessary to correct for variations. At the end of the trial the needle tip was 0.83 mm from the target.

C. 3D-Ultrasound-Guided Needle Steering Experiments

Table I lists final tip placement error for each closed-loop steering test. Over six tests using the UKF, the average error was 2.69 mm. This is within one standard deviation of the mean simulation result, and approaches an acceptable error for clinical applications. Over six tests without the UKF, the average error was 11.39 mm, which is also within one standard deviation of the mean simulation result. The robot executed between nine and twelve incremental insertions in each test.

Fig. 5 shows results from Test 1 with the UKF. In this test, the needle tip was intially located at $\boldsymbol{p} = \begin{bmatrix}-0.80 & 53.26 & -14.04\end{bmatrix}^{\mathrm{T}}$ mm, and was steered towards the target at $\boldsymbol{t} = \begin{bmatrix}-10 & 50 & 10\end{bmatrix}^{\mathrm{T}}$ mm. The figure shows the segmented needle curve, measured tip frame, and UKF-estimated tip frame after 7 UKF iterations (four initial scans and three incremental insertions). At this point the UKF-estimated tip position was close to the measured tip position; however, the UKF-estimated tip orientation was significantly different from the measured tip orientation. This example illustrates the importance of the UKF in closed-loop robot control, since using the segmentation results directly would have caused the robot to falsely correct the needle orientation with a large rotation.

IV. CONCLUSIONS/FUTURE WORK

We have demonstrated closed-loop robotic needle steering in biological tissue using medical image feedback with a clinically realistic level of measurement noise. A recursive estimation approach allows a robotic system to steer a needle along a 3D path, and position the needle tip at a target with average error of about 2 mm. We have also described experimental measurement of the variability of asymmetric-tip needle steering in *ex vivo* biological tissue. One limitation of the current approach is the reliance on kinematic models for steerable needle motion which have mostly been validated in homogeneous artificial tissues. In our future work, we will evaluate whether such kinematic models accurately capture the behavior of asymmetric-tip steerable needles in biological tissue. Overall, this estimation scheme, in combination with improved methods for needle segmentation, is an important step towards future *in vivo* needle steering.

ACKNOWLEDGMENT

The authors thank Professor Sanjay Lall for his contributions to the noise analysis.

REFERENCES

[1] K. B. Reed, A. Majewicz, V. Kallem, R. Alterovitz, K. Goldberg, N. J. Cowan, and A. M. Okamura, "Robot-assisted needle steering," *IEEE Robot. Autom. Mag.*, vol. 18, no. 4, pp. 33–46, 2011.

[2] R. J. Webster III, J. S. Kim, N. J. Cowan, A. M. Okamura, and G. S. Chirikjian, "Nonholonomic modeling of needle steering," *Int. J. Robot. Res.*, vol. 25, no. 5, pp. 509–526, 2006.

[3] M. C. Bernardes, B. V. Adorno, P. Poignet, N. Zemiti, and G. A. Borges, "Adaptive path planning for steerable needles using duty-cycling," in *IEEE Int. Conf. Robotics Automation*, 2011, pp. 2545–2550.

[4] R. Alterovitz, M. Branicky, and K. Goldberg, "Motion planning under uncertainty for image-guided medical needle steering," *Int. J. Robot. Res.*, vol. 27, no. 11–12, pp. 1361–1374, 2008.

[5] W. Park, Y. Wang, and G. S. Chirikjian, "The path-of-probability algorithm for steering and feedback control of flexible needles," *Int. J. Robot. Res.*, vol. 29, pp. 813–830, 2010.

[6] K. B. Reed, V. Kallem, R. Alterovitz, K. Goldberg, A. M. Okamura, and N. J. Cowan, "Integrated planning and image-guided control for planar needle steering," in *IEEE RAS EMBS Int. Conf. Biomedical Robotics Biomechatronics*, 2008, pp. 819–824.

[7] V. Kallem and N. J. Cowan, "Image guidance of flexible tip-steerable needles," *IEEE Trans. Robot.*, vol. 25, no. 1, pp. 191–196, 2009.

[8] D. Glozman and M. Shoham, "Image-guided robotic flexible needle steering," *IEEE Trans. Robot.*, vol. 23, no. 3, pp. 459–467, 2007.

[9] Z. Neubach and M. Shoham, "Ultrasound-guided robot for flexible needle steering," *IEEE Trans. Biomed. Eng.*, vol. 57, no. 4, pp. 799–805, 2010.

[10] M. Abayazid, R. J. Roesthuis, R. Reilink, and S. Misra, "Integrating deflection models and image feedback for real-time flexible needle steering," *IEEE Trans. Robot.*, vol. 29, no. 2, pp. 542–553, 2013.

[11] T. K. Adebar and A. M. Okamura, "3D segmentation of curved needles using Doppler ultrasound and vibration," in *Int. Conf. Information Processing Computer-Assisted Interventions*, vol. 7915, 2013, pp. 61–70.

[12] L. Crocetti, R. Lencioni, S. DeBeni, T. C. See, C. D. Pina, and C. Bartolozzi, "Targeting liver lesions for radiofrequency ablation: an experimental feasibility study using a CT-US fusion imaging system," *Invest. Radiol.*, vol. 43, no. 1, pp. 33–39, 2008.

[13] N. A. Wood, K. Shahrour, M. C. Ost, and C. N. Riviere, "Needle steering system using duty-cycled rotation for percutaneous kidney access," in *Int. Conf. IEEE EMBS*, 2010, pp. 5432–5435.

[14] A. Majewicz, J. J. Siegel, A. A. Stanley, and A. M. Okamura, "Design and evaluation of duty-cycling steering algorithms for robotically-driven steerable needles," in *IEEE Int. Conf. Robotics Automation*, 2014, pp. 5883–5888.

[15] E. Kraft, "A quaternion-based unscented Kalman filter for orientation tracking," in *Int. Conf. Information Fusion*, 2003, pp. 47–54.

[16] S. Julier and J. Uhlmann, "A new extension of the Kalman filter to nonlinear systems," in *Int. Symp. Aerospace/Defense Sensing, Simulation Controls*, 1997, pp. 182–193.

[17] S. Thrun, W. Burgard, and D. Fox, *Probabilistic Robotics*. MIT Press, 2005.